Iranian Journal of Chemical Engineering

Journal Homepage: www.ijche.com

pISSN: 1735-5397
eISSN: 2008-2355

Comparative Assessment of Stress-Strain Field of BLISK and Fir-Tree Turbine Blade Roots in the Ti-6Al-4V Alloy as a Prerequisite for Fatigue Life Prediction

Ali Reza Sharifi Nezhad [1], Armin Sabetghadam-Isfahani [2], Yegane Davoodbeygi [3]*, Seyed Mahmood Latifi [4], Abdolhossein Barzin [2]

[1] National Iranian Gas Company, Tehran, Iran.
[2] Department of Safety Engineering and Technical Inspection, Faculty of Chemical and Petroleum Engineering,University of Hormozgan, Bandar-Abbas, Iran.
[3] Department of Chemical Engineering, Faculty of Chemical and Petroleum Engineering, University of Hormozgan, Bandar-Abbas, Iran.
[4] Corrosion Engineering and Material Protection Department, Amirkabir University of Technology, Bandar-Abbas, Iran.

ARTICLE INFO

Article type:
Research article

Article history:
Received: 2026-04-20
Revised: 2026-05-30
Accepted: 2026-06-25
Available online: 2026-06-30

Keywords:
Ti-6Al-4V,
BLISK,
Fir-tree analysis,
Finite Element Analysis (FEA)

ABSTRACT

Modern steam turbines employ extended low-pressure blades, subjecting root connections to severe centrifugal and thermal loads. As a result of these loadings, various and severe dynamic stresses are formed in the structure. Understanding the distribution of these stresses and conducting studies on it will greatly help determine the lifespan of items and how to manage them. This study evaluates stress and strain distributions in Ti-6Al-4V turbine roots, specifically comparing BLISK and fir-tree designs under operational conditions. Using the nonlinear Finite Element Analysis (FEA) and Local Plastic Stress and Strain Analysis (LPSA), the peak von Mises stress was identified as 890.76 MPa for the BLISK and 390.82 MPa for fir-tree roots. Advanced damage frameworks, including the Modified Mohr-Coulomb and Lemaitre's CDM models, are discussed conceptually to identify critical stress triaxiality states, thereby establishing a reliable baseline for subsequent fracture analyses. The findings establish a reliable baseline for fatigue studies, identifying root-blade transition fillets as critical sites for low-cycle fatigue failure. Understanding the behavior of materials under fatigue loading can help in better determining the scope of application of the design and optimizing it.

DOI: 10.22034/ijche.2026.579155.1588 URL: https://www.ijche.com/article_250374.html

*Corresponding author: y.davoodbeygi@hormozgan.ac.ir

1. Introduction

The global demand for high-efficiency steam turbines has surged significantly in recent years, driven by rising electricity costs and increasingly stringent environmental regulations. To maximize performance and reduce exhaust loss, manufacturers have moved toward extending the length of the end low-pressure (LP) blades. However, as airfoils become longer and more massive to maintain dynamic stability, the blade-disc connection is subjected to increasingly severe centrifugal forces [1]. Modern turbine blades operate under demanding mechanical and thermal conditions, where high rotational speeds, elevated temperatures, and complex boundary constraints generate significant localized stress, particularly in the root regions [2].

Specialized designs such as fir-tree and BLISK (Bladed Disk) configurations are widely adopted for their structural efficiency and effective load transfer, though these geometries can produce localized stress concentrations that strongly influence overall durability [3-6]. For these high-performance rotating components, the Ti-6Al-4V titanium alloy is the material of choice across the aerospace, power generation, and oil and gas industries. This $\alpha+\beta$ alloy accounts for more than 50% of total titanium usage due to its optimal balance of high specific strength, low density, and excellent corrosion resistance [7]. The microstructure of the alloy typically features $\alpha+\beta$ phases with an average grain size of approximately 20μm, supporting the robust performance and creep resistance at elevated temperatures [7-9].

In operational environments, turbine blade materials typically enter local plasticity at operational speeds. As turbines are repeatedly started up and shut down, varying centrifugal forces create repeated plastic strain, leading to crack initiation and low cycle fatigue (LCF) failure [1, 10]. Unlike high-cycle fatigue (HCF), which is associated with vibrational resonance, LCF is the dominant life-limiting factor for blade roots because the stress concentrations at fillets and contact surfaces exceed the yield strength during each startup/shutdown cycle [1, 2]. Therefore, fatigue-based assessments, specifically in LCF criteria, provides the most relevant framework for evaluating the structural integrity of these critical components. Establishing a clear understanding of stress-strain fields provides essential input for advanced life prediction methods, helping engineers design blades that are both lightweight and durable [11].

To accurately predict structural lifetime and verify design integrity, researchers employ the Nonlinear Finite Element Analysis (FEA) and Local Plastic Stress and Strain Analysis (LPSA). The LPSA method utilizes the real elastic-plastic state of stress and strain at critical nodes as fundamental input to determine cycles to crack initiation. The uniaxial Smith, Topper, Wetzel (SWT) damage parameter is frequently applied, utilizing material parameters from Manson-Coffin curves, Young's modulus, and stress-strain amplitudes [1].

Beyond the structural fatigue analysis, the comprehension of the damage behavior of materials is vital for defining criteria that reduce the risk and cost of catastrophic structural failures. Ductile damage models are generally classified into three groups: phenomenological models, porosity models, and continuum damage mechanics (CDM) models [7]. Phenomenological models, such as the Johnson–Cook [12], Rice–Tracey [13], Leroy et al. [14] and Cockroft–Latham criteria [15], are widely used in industrial applications due to their relatively simple calibration procedures. These models are typically uncoupled, assuming that the damage process does not affect the plastic behavior of materials; failure occurs abruptly when a damage parameter reaches a critical threshold [8, 16-24]. Porosity models like the Gurson–Tvergaard–Needleman (GTN) model offer a micromechanical approach but are significantly more complex to calibrate, requiring the determination of nine separate parameters [25-27].

Recent advancements highlight that stress triaxiality and Lode angle play critical roles in ductile fracture [22, 24]. While triaxiality accounts for the effects of pressure on fracture, the Lode angle describes the relationship between the intermediate principal stress and minor/major principal stresses [7]. The Modified Mohr-Coulomb (MMC) damage criterion considers both effects, transforming the fracture locus from a 2D curve into a 3D surface defined by triaxiality, Lode angle, and failure strain and demonstrating promising results under extreme load conditions [18, 19]. A parallel framework, notably Lemaitre's model, is Continuum Damage Mechanics (CDM) [28]. Unlike uncoupled phenomenological models, CDM models couple plasticity and damage through a continuous parameter D that evolves during loading, accounting for the progressive changes in the shape and number of voids [7, 28-30]. Calibration requires reverse methods comparing experimental data from various geometries with numerical simulations [7].

A persistent challenge in modern damage modeling is geometry transferability, where models calibrated for one configuration may lead to relevant errors when extended to other scenarios [31]. Practitioners must also consider mesh size sensitivity, particularly in specimens with sharp notches, where decreasing mesh size often results in earlier predicted displacement at failure [21, 32]. Establishing reliable baselines through the extensive experimental testing and FEA verification is essential for ensuring numerical predictions accurately reflect physical phenomena [7].

This study presents a finite element investigation of stress and strain distributions in Ti-6Al-4V turbine blade roots, considering combined effects of the rotational speed, thermal loading, and mechanical constraints. The primary goal is to perform a comparative static structural assessment, identifying critical stress concentration zones and generating high-fidelity strain fields, which serve as a prerequisite baseline (geometry validation and mesh convergence) for subsequent detailed low-cycle fatigue and damage-evolution analyses.

2. Materials and Methods

2.1. Material characterization

Ti-6Al-4V is a widely used α+β titanium alloy, providing an optimal balance of high strength, low density, corrosion resistance, and excellent performance at elevated temperatures. This alloy accounts for more than 50% of the total titanium usage globally and is extensively employed in turbine blades for aerospace, as well as in high-performance rotating components in power generation and oil and gas industries. The microstructure of the material consists of clearly visible α+β phases with an average grain size of approximately 20μm, as illustrated in Figure 1 [7].

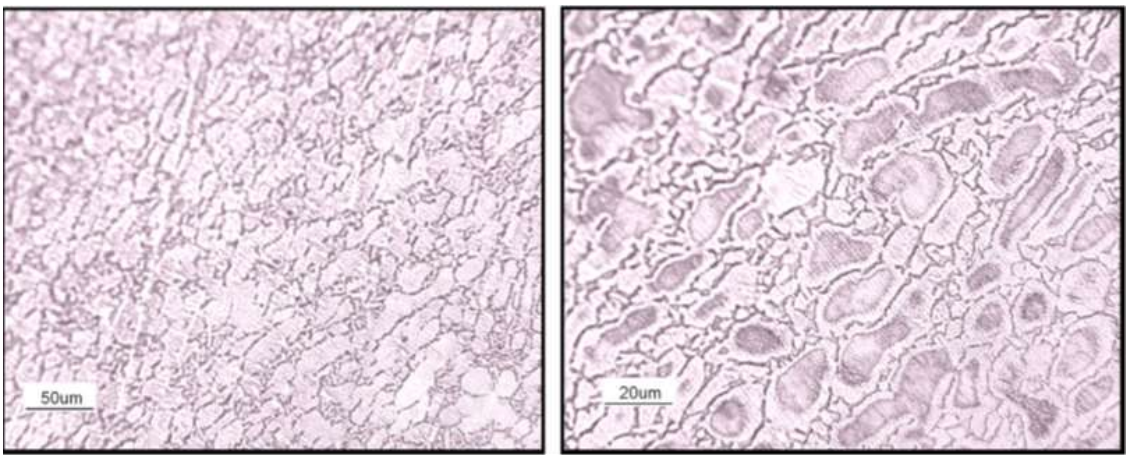

(a) **(b)**

Figure 1. Microstructure of the tested Ti–6Al–4V titanium alloy showing α+β phases at (a) 200× and (b) 500× magnification [4].

The chemical composition of Ti-6Al-4V by weight is essential for establishing its mechanical baseline and is summarized in Table 1. The detailed composition analysis indicates trace elements including Oxygen (0.16%), Nitrogen (0.01%), Carbon (0.01%), Hydrogen (0.001%), and Iron (0.15%).

Table 1.
Weight chemical composition of the Ti–6Al–4V titanium alloy.

Ti-6Al-4V		
Titanium (Ti)	Aluminum (Al)	Vanadium (V)
90%	6%	4%

The density of the alloy is illustrated in Figure 2 and detailed across a temperature range of 20 °C to 2500 °C in Table 2. The melting temperature is 1605 °C, and the zero-thermal-strain reference temperature is 19.85 °C, which are key parameters for evaluating thermal responses under operational conditions. Temperature-dependent thermal properties, including the coefficient of thermal expansion (Table 3), orthotropic thermal conductivity (Table 4), and specific heat at constant pressure (Table 5), play a crucial role in determining thermal strains during service.

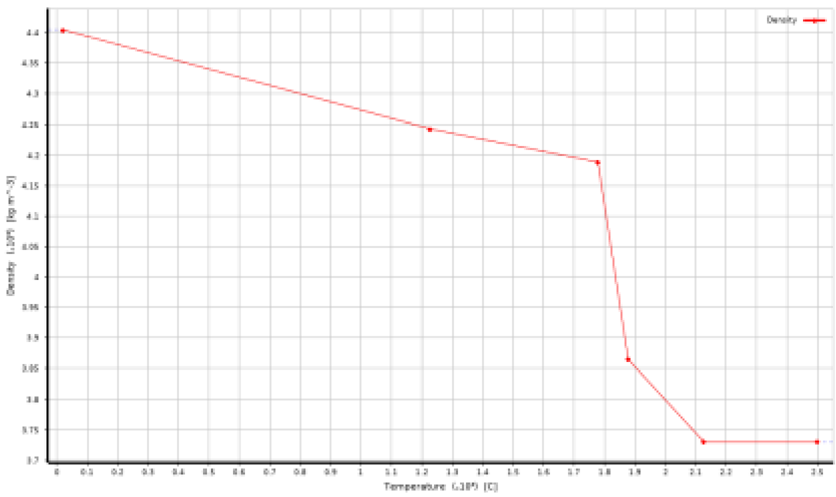

Figure 2. Temperature-dependent density distribution of Ti-6Al-4V utilized in the finite element analysis.

Table 2.
Density of Ti-6Al-4V across a temperature range of 20 °C to 2500 °C.

	Temperature (C)	Density
1	20	4405
2	1227	4243
3	1777	4189
4	1877	3865
5	2127	3730
6	2500	3730

Table 3.
Isotropic secant coefficient of the thermal expansion for Ti-6Al-4V at various temperatures.

	Temperature (C)	Coefficient of Thermal Expansion (C^{-1})
1	-233.15	6.5E-06
2	-173.15	7.1E-06
3	19.85	8.9E-06
4	126.85	9.7E-06
5	326.85	1.08E-05
6	526.85	1.14E-05
7	626.86	1.16E-05
8	826.86	1.16E-05

Table 4.
Orthotropic thermal conductivity of Ti-6Al-4V in X, Y, and Z directions as a function of temperature.

Thermal Conductivity X Direction W mm^-1 K^-1	Thermal Conductivity Y Direction W mm^-1 K^-1	Thermal Conductivity Z Direction W mm^-1 K^-1	Temperature K
8.11e-003	8.11e-003	7.01e-003	293.15
7.74e-003	7.74e-003	7.34e-003	373.15
7.52e-003	7.52e-003	8.02e-003	473.15
7.55e-003	7.55e-003	8.95e-003	573.15
7.81e-003	7.81e-003	1.007e-002	673.15
8.29e-003	8.29e-003	1.136e-002	773.15
8.96e-003	8.96e-003	1.275e-002	873.15
9.81e-003	9.81e-003	1.421e-002	973.15
1.082e-002	1.082e-002	1.568e-002	1073.2
1.198e-002	1.198e-002	1.714e-002	1173.2
1.326e-002	1.326e-002	1.852e-002	1273.2
1.465e-002	1.465e-002	1.978e-002	1373.2
1.613e-002	1.613e-002	2.088e-002	1473.2
1.769e-002	1.769e-002	2.177e-002	1573.2
1.929e-002	1.929e-002	2.242e-002	1673.2
2.093e-002	2.093e-002	2.276e-002	1773.2
2.26e-002	2.26e-002	2.276e-002	1873.2
2.853e-002	2.853e-002	2.853e-002	1923.2
2.945e-002	2.945e-002	2.945e-002	1973.2
3.128e-002	3.128e-002	3.128e-002	2073.2
3.311e-002	3.311e-002	3.311e-002	2173.2
3.402e-002	3.402e-002	3.402e-002	2223.2

Table 5.
Temperature-dependent specific heat at constant pressure for Ti-6Al-4V.

Specific Heat mJ kg^-1 K^-1	Temperature (K)
5.4267e+005	20
5.5206e+005	100
5.6586e+005	200
5.8158e+005	300
5.9882e+005	400
6.172e+005	500
6.753e+005	800
7.1258e+005	1000
7.7796e+005	1500

Table 6.
Temperature-dependent bilinear isotropic hardening parameters for Ti-6Al-4V.

	Temperature (C)	Yield Strength (Pa)	Tangent Modulus (Pa)
1	20	1098000000	1332000000
2	204	844000000	1207000000
3	427	663000000	1033000000
4	538	527000000	943000000
5	815	60000000	708000000
6	944	21000000	596000000

The mechanical response of Ti-6Al-4V is initially isotropic and elastic up to the yield point, beyond which plastic deformation occurs following a bilinear hardening law. This behavior is quantified in Table 6, where the yield strength is shown to decrease from 1098 MPa at 20 °C to 21 MPa at 944 °C. Elastic properties, such as Young's Modulus and Poisson's Ratio across various temperatures, are detailed in Table 7. The ultimate tensile strength of the material is 950 MPa.

The fatigue behavior of the alloy is represented by the S-N curve in Figure 3, which provides the basis for the high-cycle fatigue analysis. Numerical values for alternating stress versus loading cycles are provided in Table 8.

Table 7.
Isotropic elastic properties of Ti-6Al-4V across a wide thermal range (293.15 K to 1873.2 K).

Young's Modulus MPa	Poisson's Ratio	Bulk Modulus MPa	Shear Modulus MPa	Temperature K
1.07e+005	0.323	1.0075e+005	40438	293.15
1.034e+005	0.328	1.0019e+005	38931	373.15
99510	0.334	99910	37298	473.15
93710	0.339	97008	34993	573.15
85500	0.345	91935	31784	673.15
74710	0.351	83568	27650	773.15
61840	0.357	72075	22786	873.15
48160	0.363	58589	17667	973.15
35290	0.369	44898	12889	1073.2
24500	0.374	32407	8915.6	1173.2
16290	0.38	22625	5902.2	1273.2
10490	0.386	15336	3784.3	1373.2
6610	0.392	10201	2374.3	1473.2
4106	0.398	6709.2	1468.5	1573.2
2528	0.403	4343.6	900.93	1673.2
1547	0.409	2833.3	548.97	1773.2
943.5	0.415	1850	333.39	1873.2

Table 8.
Fatigue life data for Ti-6Al-4V: Alternating stress vs. loading cycles.

	Cycles	Alternating Stress (MPa)
1	1000	950
2	10000	820
3	100000	620
4	1000000	520
5	10000000	470
6	100000000	420

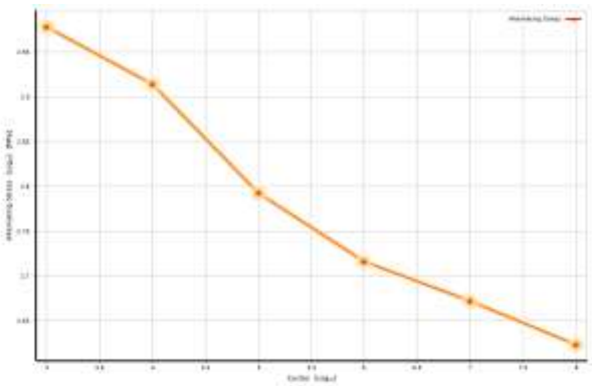

Figure 3. High-cycle fatigue behavior of Ti-6Al-4V represented by the S-N curve.

2.2. Computational methodology

The structural integrity of high-performance turbine components is evaluated using an integrated computational approach combining advanced numerical modeling with the localized damage assessment. The determination of the stress and strain distribution at the blade root is performed using nonlinear FEA. For material characterization, 8-node brick elements with reduced integration (C3D8R) are adopted, as they provide excellent results in simulating complex stress states of Ti-6Al-4V. The LPSA method serves as the fundamental framework for predicting fatigue onset, using the real elastic-plastic state calculated at critical nodes as primary input [1].

To account for multiaxial stress states inherent in rotating components, the von Mises rule is used to reduce triaxial stress and strain components. The von Mises criterion is selected because Ti-6Al-4V is a ductile material, and this criterion provides a reliable scalar equivalent stress for predicting yielding and plastic deformation under multiaxial loadings. Its widespread acceptance in turbine design standards and its consistency with the material's yield strength data (Table 6) further justify its application in this study. The advanced damage characterization considers stress triaxiality and Lode angle, which describe relationships between principal stresses and are critical for defining the fracture loci of ductile metals [1, 7]. The von Mises equivalent stress is defined as:

$$\sigma_{VM} = \sqrt{\frac{(\sigma_1-\sigma_2)^2+(\sigma_2-\sigma_3)^2+(\sigma_3-\sigma_1)^2}{2}} \quad (1)$$

where σ_1, σ_2, and σ_3 are the principal stresses. This scalar invariant provides a single equivalent stress value for comparison with the yield strength of the material in ductile materials such as Ti-6Al-4V.

2.3. BLISK analysis

The BLISK (Bladed Disk) configuration integrates the blade and disk into a single component, significantly reducing stress risers by eliminating mechanical joints. The operational and geometrical parameters for the BLISK structure are detailed in Table 9.

Table 9.
Operational and geometrical parameters of the BLISK blade structure.

Parameter	Value	Unit
Number of blades	20	-
Total structure weight	206.33	kg
Total structure volume	0.0468	m³
Rotational speed	11500	RPM
Number of cycles	5750	-
Operating pressure	0.5	MPa
Operating temperature	300	°C

2.4. Fir-tree configuration

The fir-tree design utilizes interlocking profiles to transfer loads to the disk while allowing individual blade replacement. The operational parameters for the 36-blade fir-tree assembly are summarized in Table 10.

Table 10.
Operational and geometrical parameters of the Fir-tree blade structure.

Parameter	Value	Unit
Number of blades	36	-
Total structure weight	14.47	kg
Total structure volume	0.00328	m³
Rotational speed	11500	RPM

2.5 Theoretical framework for future damage and fatigue modeling

To establish a baseline for fatigue studies, loading cycles unitl crack initiation are predicted using the uniaxial Smith, Topper, Wetzel (SWT) damage parameter, incorporating the Manson-Coffin curve constants, stress amplitudes, and mean stress. Because turbine materials enter a state of localized plasticity at operating speeds, varying centrifugal forces during startup/shutdown cycles lead to repeated plastic strain [1]. The SWT parameter is defined as:

$$SWT = \sigma_{max} \cdot \varepsilon_a \quad (2)$$

where σ_{max} is the maximum stress and ε_a is the strain amplitude. The fatigue life is then related to the SWT parameter through the Manson-Coffin relationship:

$$SWT = \frac{\left(\sigma_f'\right)^2}{E}\left(2N_f\right)^{2b} + \sigma_f'\varepsilon_f'\left(2N_f\right)^{b+c} \quad (3)$$

where σ'f is the fatigue strength coefficient, b is the fatigue strength exponent, ε'f is the fatigue ductility coefficient, c is the fatigue ductility exponent, E is the Young's modulus, and Nf is the number of cycles to failure. This formulation allows the estimation of the fatigue initiation life from the computed stress and strain amplitudes at critical locations [1, 11].

This framework utilizes the Modified Mohr-Coulomb (MMC) and Lemaitre's CDM models to evaluate how the localized stress states and material deterioration affect long-term durability. The MMC criterion considers both stress triaxiality and Lode angle effects, transforming the fracture locus from a 2D curve into a 3D surface defined by triaxiality, Lode angle, and failure strain. The Lemaitre's CDM model couples plasticity and damage through a continuous parameter D that evolves during loading, accounting for progressive changes in the shape and number of voids [1, 7, 33].

It is important to emphasize that the MMC and Lemaitre CDM models are introduced here as the conceptual foundation for the ongoing research programme. Their practical implementation - including the damage evolution contours, fracture surface predictions, and calibration of model-specific parameters - requires dedicated geometry-specific experimental validation and nonlocal regularization techniques to overcome mesh sensitivity. These steps are beyond the scope of the present baseline study and are explicitly outlined as the primary objectives of our subsequent experimental phase (Section 3.6).

3. Results and discussion

3.1. BLISK structural response

The finite element results for the BLISK structure show that the maximum total deformation occurs at the blade tips, reaching a peak of 10.447 mm, as illustrated in Figure 4. This deformation pattern is consistent with the effects of centrifugal forces, with values gradually decreasing toward the relatively stiff root region.

The corresponding stress analysis reveals that the highest von Mises stress reaches 890.76 MPa. As shown in Figure 5, these stresses are concentrated in three critical locations: near the cylindrical support attachment, the midsection of the root (indicating bending and torsional effects), and the root-blade transition fillet. These fillets are particularly susceptible to localized stress amplification due to geometric discontinuities.

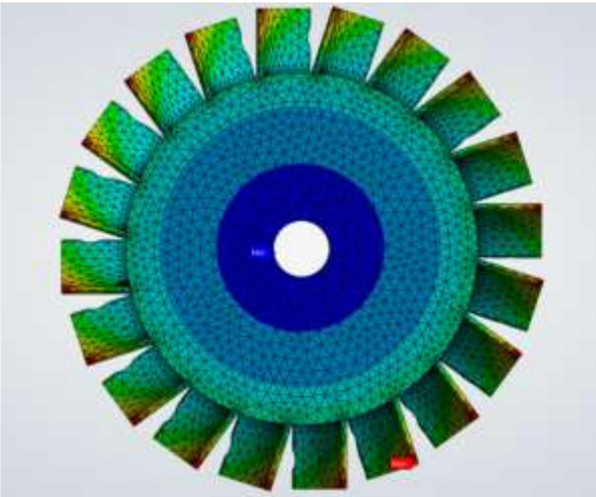

Figure 4. Total deformation of the BLISK blade structure under operational loading conditions.

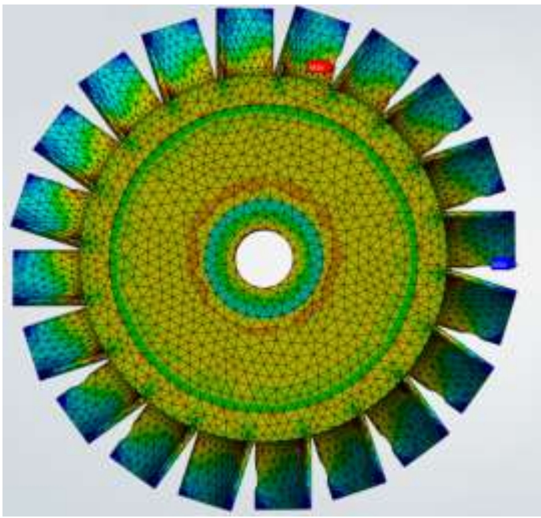

Figure 5. Von-Mises stress distribution of the BLISK blade structure under operational loadings.

3.2. Fir-tree structural response

Similar to the same in the BLISK configuration, the maximum deformation in the fir-tree blade occurs at the tip, totaling 0.664 mm, as depicted in Figure 6. The interlocking geometry effectively distributes the load across the segments.

The stress distribution analysis, presented in Figure 7(a) (blade portion) and Figure 7(b) (root portion), identifies a peak von Mises stress of 390.82 MPa. The maximum stress is observed at the root-blade fillets, confirming that while the blades experience significant deformation, the root is the most critical location for potential fatigue and structural failure.

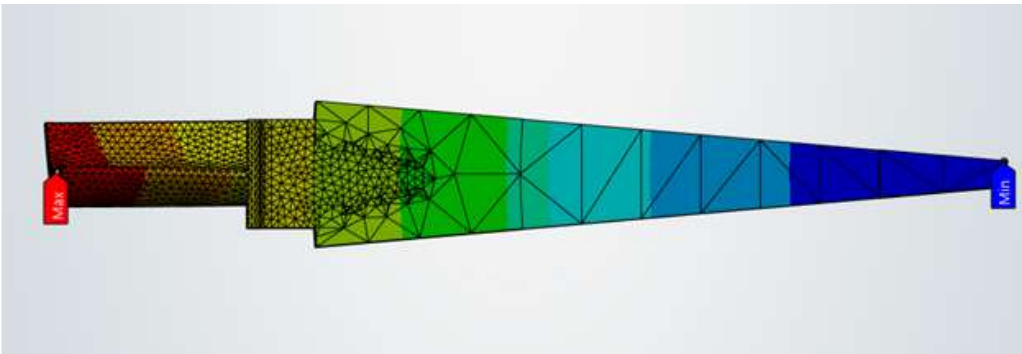

Figure 6. Total deformation of the simulated Fir-tree blade under operational loading conditions.

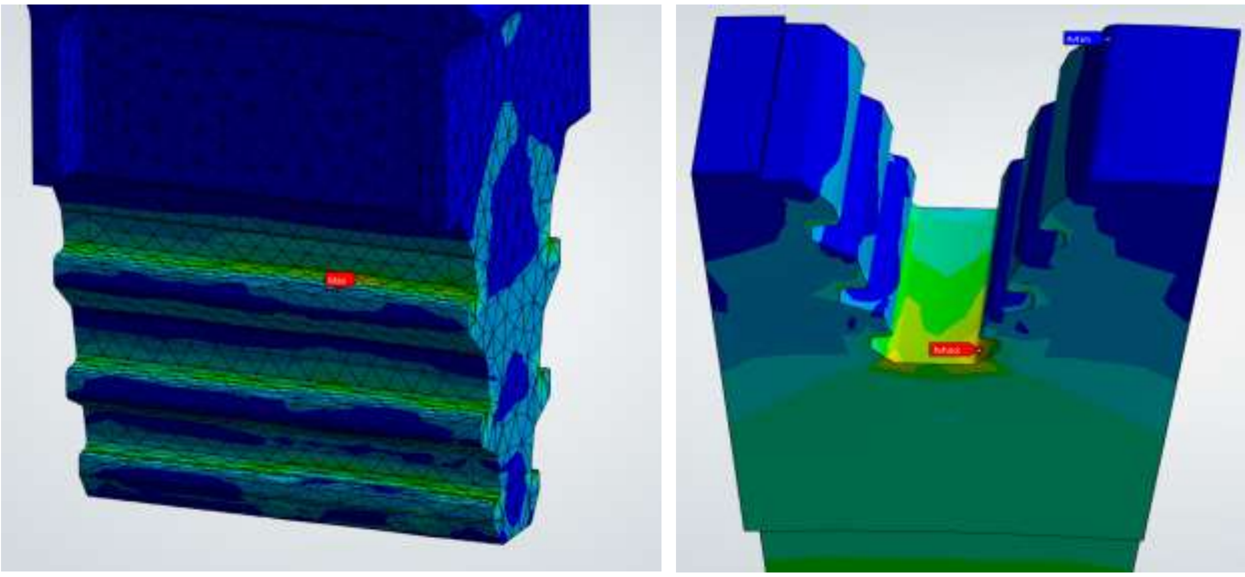

(a) **(b)**

Figure 7. (a) Von-Mises stress distribution on the blade portion, (b) Von-Mises stress distribution on the root.

3.3. Comparative analysis

Structural simulations reveal that while maximum deformations occur at blade tips (reaching 10.447 mm for BLISK and 0.664 mm for fir-tree assemblies) the most critical regions for structural integrity are localized at geometric discontinuities. Specifically, the peak von Mises stresses of 890.76 MPa in BLISK and 390.82 MPa in fir-tree roots were identified at root-blade transition fillets. These findings confirm that the root is the primary site for potential LCF failure due to the localized stress amplification and repeated plastic strain during turbine startup and shutdown cycles.

The stress concentration at these fillets is primarily attributed to the abrupt change in the cross-sectional geometry, which disrupts the uniform transmission of centrifugal load paths and forces stress lines to converge [3]. The monolithic BLISK structure transmits the full cyclic load directly to this junction, while the fir-tree design combines sharp geometric notches with local Hertzian contact stresses at the contact surfaces, further amplifying the local stress field.

It is crucial to explicitly acknowledge that the BLISK and Fir-tree models differ substantially in total mass (206.33 kg vs. 14.47 kg) and blade count (20 vs. 36). Therefore, the absolute peak stress values (890.76 MPa vs. 390.82 MPa) are not directly comparable in a quantitative sense. The comparison presented here is intentionally qualitative and mechanistic, focusing on identifying common critical zones (root-blade transition fillets) and contrasting the distinct load-transfer mechanisms (monolithic vs. interlocking).

To provide a more equitable quantitative perspective, the peak von Mises stresses were normalized by their respective structural masses. This normalization yields approximately 4.32 MPa/kg for the BLISK configuration (890.76 MPa / 206.33 kg) and 27.01 MPa/kg for the Fir-tree configuration (390.82 MPa / 14.47 kg). This mass-normalized indicator reveals that, although the Fir-tree design exhibits a lower absolute peak stress, it experiences significantly higher stress per unit mass—approximately 6.3 times that of the BLISK—highlighting its distinct mechanical response and higher relative stress concentration efficiency under the same rotational speed. A truly equivalent comparison would require identical blade counts and mass, which lies beyond the scope of this foundational study.

Based on the qualitative and mass-normalized comparisons, neither design is claimed to be absolutely superior to the other; rather, each exhibits distinct structural characteristics and failure-susceptibility patterns that must be considered within its respective design contexts.

The fir-tree root does experience notable local stress concentrations at the contact surfaces and fillets, consistent with the extensive literature on turbines. The lower absolute peak stress (390.82 MPa) compared to that of the BLISK design (890.76 MPa) is primarily a consequence of the substantially lower total mass (14.47 kg vs. 206.33 kg) and blade count (36 vs. 20), not an indication that stress concentrations are absent in the fir-tree design.

3.4. Fatigue life prediction

To provide a preliminary quantitative benchmark, the peak von Mises stresses obtained from the static FEA (890.76 MPa for BLISK and 390.82 MPa for Fir-tree) were treated as the cyclic alternating stress (σ_a) in a conservative first-order estimation. By the logarithmic interpolation of the material's empirical S-N curve (Table 8) between 1,000 cycles (950 MPa) and 10,000 cycles (820 MPa), the estimated crack-initiation life for the BLISK configuration is approximately 2,700 cycles (precisely 2,734 cycles), whereas the Fir-tree configuration, with a peak stress well below the 10^7-cycle endurance limit (470 MPa), falls into the infinite life regime ($>10^7$ cycles).

It must be emphasized that these are uniaxial, first-order approximations derived from von Mises equivalence and the Manson-Coffin/SWT framework. They are presented solely as a quantitative baseline to highlight the relative susceptibility of the two designs. The calculation of the actual SWT parameter from cyclic hysteresis data, along with definitive multiaxial life predictions, requires dedicated strain-controlled fatigue testing, nonlocal regularization, and experimental validation—all of which are outlined as future work in Section 3.6.

3.5. Limitations

The present numerical framework is subject to several inherent limitations that must be acknowledged when interpreting the results. First, the geometry transferability of the employed damage models presents a significant constraint. The MMC and Lemaitre-type damage models were calibrated using standard laboratory specimens (smooth, notched, and flat); therefore, their direct transfer to the highly complex geometry and multiaxial stress fields of BLISK and fir-tree roots remains approximate and may generate noticeable errors if the local triaxiality–Lode state deviates from the calibration space. This geometry transferability problem is recognized as a persistent challenge in modern damage modeling, where a model calibrated for one configuration may lead to relevant errors when extended to other scenarios [34].

Second, the fatigue-life predictions based on the SWT parameter tend to be conservative with respect to real components. This conservatism arises because the current framework does not explicitly capture strong strain-gradient effects or load-history-dependent residual stresses. Neglecting these factors (including strain-gradient effects in notched regions and the beneficial redistribution effects of residual stresses due to plasticity during initial overload cycles) results in predicted numbers of cycles to crack initiation that are shorter than experimentally observed values. While this provides a safety margin for industrial design purposes, it may lead to over-engineering and non-optimal maintenance scheduling if not properly validated against experimental data [35, 36].

Third, the finite-element response in sharply notched regions is inherently sensitive to mesh refinement, and the ductile damage models themselves are known to exhibit pathological mesh dependence in the absence of explicit regularisation. Decreasing mesh size often results in the earlier prediction of displacement at failure, so that peak stresses and failure displacements should be regarded as engineering indicators of mesh qualification rather than as fully objective quantities. Without systematic mesh-convergence studies, the reported stress values (such as the peak von Mises stresses of 890.76 MPa and 390.82 MPa) contain inherent uncertainty dependent on the selection of element size.

3.6 Recommendations for Future Work

To address the limitations identified in the present study, the following specific priorities are recommended for future work:

1) Experimental calibration of MMC and Lemaitre CDM models: Application-specific specimens (e.g., notched and flat-grooved geometries) should be designed to reproduce the actual stress triaxiality and Lode angle conditions prevailing at the root-blade transition fillets. These will enable the reliable calibration of the fracture loci and the damage evolution parameter (D) for the Ti-6Al-4V alloy under turbine-relevant loading paths.

2) Damage evolution contours and crack-growth simulations: Once calibrated, the Lemaitre CDM model can be implemented to generate progressive damage contours and to simulate crack initiation and subsequent propagation using cohesive zone or extended finite element methods (XFEM) in the critical fillet regions.

3) Refined fatigue-life prediction using SWT parameter: While the present study provides a preliminary life estimate via S-N interpolation, future work should compute the full Smith-Watson-Topper (SWT) parameter directly from the cyclic stress-strain hysteresis loops obtained from advanced material testing (e.g., strain-controlled LCF tests). This will replace the current conservative first-order approximation with a multiaxial, cycle-by-cycle fatigue assessment.

4) Mesh-objective regularisation: To overcome the inherent mesh sensitivity of local damage models, the nonlocal formulations of gradient-enhanced or integral type should be adopted, ensuring that damage contours and failure displacements are independent of element size.

5) Sub-modelling strategy: Global wheel models should be coupled with the highly refined local sub-models of the root fillets to capture the stress gradients with greater accuracy without excessive computational cost.

4. Conclusion

This investigation successfully established a comprehensive static finite-element baseline for stress and strain distributions in Ti-6Al-4V turbine blade roots, providing critical insights into the localization of stress and plastic strain concentrations. Furthermore, the theoretical applicability of MMC and Lemaitre-type models was evaluated in the context of the identified stress triaxiality states, confirming their qualitative suitability for future implementation in the subsequent phase of this research programme.

Key findings include:

- Root-blade transition fillets are the primary sites for potential LCF failure due to localized stress amplification
- BLISK configurations exhibit higher peak stresses (890.76 MPa) compared to fir-tree designs (390.82 MPa)
- MMC and Lemaitre CDM models are introduced as a theoretical framework for future damage characterization, but their practical implementation requires careful calibration for specific stress states and geometry-specific validation
- Mesh sensitivity and geometry transferability remain significant challenges requiring regularization techniques and application-specific calibration

It is emphasized that the comparative assessments presented in this work are qualitative and relative; based on the observed structural responses, neither the BLISK nor the Fir-tree configuration is claimed to be absolutely superior to the other. Instead, each exhibits distinct mechanical characteristics and failure-susceptibility patterns that are specific to its respective design philosophy and scale.

The experimental verification, using strain gauge measurements on scaled fir-tree models, confirmed FEA correctness, with measured values corresponding closely to calculated strains. While numerical lifetime predictions tend to be conservative, they provide reliable safety margins for industrial designs.

For practical industrial applications, calibration tests should be performed under stress states (triaxiality and Lode angle) closely resembling real applications to minimize geometry-transferability errors. This study establishes necessary foundational data for subsequent fatigue and fracture investigations, ensuring the continued safety and efficiency of high-speed rotating turbine assemblies.

References

[1]Měšťánek P, Kubín Z (2010) Fatigue testing of the fir tree root of a turbine blade. Experimentální analýza napětí, 261-268.

[2]Robertson M, Walton D (1990), A design analysis of steam turbine blade roots under centrifugal loading, The Journal of Strain Analysis for Engineering Design, 25: 185-195. https://journals.sagepub.com/doi/abs/10.1243/03093247V253185.

[3]Yuan R, Liao D, Zhu S. P., Yu Z. Y., Correia J, De Jesus A (2021), Contact stress analysis and fatigue life prediction of turbine disc–blade attachment with fir-tree tenon structure, Fatigue and Fracture of Engineering Materials and Structures, 44: 1014-1026. https://doi.org/10.1111/ffe.13410.

[4]Li H, Chen L, Chen C. H., Fei C (2024), Design Optimization Approach of Functionally Graded Turbine Blisk, 2024 10th Asia Conference on Mechanical Engineering and Aerospace Engineering (MEAE), 222-227. 10.1109/MEAE62008.2024.11026622.

[5]Kelly S. T., Epureanu B. I. (2025), Physics-informed machine learning approach for reduced-order modeling of integrally bladed rotors: Theory and application, Journal of Sound and Vibration, 596: 118-133. https://doi.org/10.1016/j.jsv.2024.118773.

[6]Hashemi M, Aghaei M (2023), Fatigue Endurance Optimization of a Steam Turbine Blade Curved Fir-Tree Root, Journal of Stress Analysis, 7: 281-301 . 10.22084/jrstan.2023.27108.1228.

[7] Allahverdizadeh N, Gilioli A, Manes A, Giglio M (2015), An experimental and numerical study for the damage characterization of a Ti–6AL–4V titanium alloy, International Journal of Mechanical Sciences, 93: 32-47. https://doi.org/10.1016/j.ijmecsci.2015.01.005.

[8] Giglio M, Manes A, Viganò F (2012), Numerical simulation of the slant fracture of a helicopter's rotor hub with ductile damage failure criteria, Fatigue & Fracture of Engineering Materials & Structures, 35: 317-327. https://doi.org/10.1111/j.1460-2695.2011.01622.x.

[9] Gao Z, Zhu C, Shu Y, Wang S, Wang C, Chen Y (2024), Predicting the low-cycle fatigue life of Ti-6Al-4V alloy using backpropagation neural network optimized by the improved dung beetle algorithm, Fatigue and Fracture of Engineering Materials and Structures, 47: 3983-3999. https://doi.org/10.1111/ffe.14407.

[10] Manzini F, Cesaretti A, Bessone A, Bagnera F, Botto D (2024), Lifing assessment of Gas Turbine blade root affected by Out-of-Tolerances, Materials, 17: 4881. https://doi.org/10.3390/ma17194881.

[11] Lan J, Dai B, Wei J, Yao W, Yu P (2024), Structural Design and Life Prediction of Sheet Metal Parts for Gas Turbine Vane, Journal of Physics: Conference Series, 2706 (1): 012030. https://doi.org/10.1088/1742-6596/2706/1/012030.

[12] Johnson G. R., Cook W. H. (1985), Fracture characteristics of three metals subjected to various strains, strain rates, temperatures and pressures, Engineering fracture mechanics, 21: 31-48. https://doi.org/10.1016/0013-7944(85)90052-9.

[13] Rice J. R., Tracey D. M. (1969), On the ductile enlargement of voids in triaxial stress fields∗, Journal of the Mechanics and Physics of Solids, 17: 201-217. https://doi.org/10.1016/0022-5096(69)90033-7.

[14] Le Roy G, Embury J, Edwards G, Ashby M (1981), A model of ductile fracture based on the nucleation and growth of voids, Acta Metallurgica, 29: 1509-1522. https://doi.org/10.1016/0001-6160(81)90185-1.

[15] Cockcroft M, Latham D. J (1968), Ductility and workability of metals, Journal of the Institute of Metals, 96: 24-44. https://www.scirp.org/reference/referencespapers?referenceid=628413.

[16] Bao Y, Wierzbicki T (2004), A comparative study on various ductile crack formation criteria, Journal of Engineering Materials and Technology., 126: 314-324. https://doi.org/10.1115/1.1755244.

[17] Bao Y, Wierzbicki T (2004), On fracture locus in the equivalent strain and stress triaxiality space, International journal of mechanical sciences, 46: 81-98. https://doi.org/10.1016/j.ijmecsci.2004.02.006.

[18] Bai Y, Wierzbicki T (2008), A new model of metal plasticity and fracture with pressure and Lode dependence, International journal of plasticity, 24: 1071-1096. https://doi.org/10.1016/j.ijplas.2007.09.004.

[19] Bai Y, Wierzbicki T (2010), Application of extended Mohr–Coulomb criterion to ductile fracture, International journal of fracture, 161: 1-20. https://link.springer.com/article/10.1007/s10704-009-9422-8.

[20] Giglio M, Manes A, Vigano F (2012), Ductile fracture locus of Ti–6Al–4V

titanium alloy, International Journal of Mechanical Sciences, 54: 121-135. https://doi.org/10.1016/j.ijmecsci.2011.10.003.

[21] Gilioli A, Manes A, Giglio M (2014), Numerical simulation of a fracture toughness test of an Al6061-T6 aluminium alloy using a ductile criterion, Mechanics Research Communications, 58: 2-9. https://doi.org/10.1016/j.mechrescom.2013.08.007.

[22] Gao X, Zhang G, Roe C (2010), A study on the effect of the stress state on ductile fracture, International Journal of Damage Mechanics, 19: 75-94. https://doi.org/10.1177/1056789509101917.

[23] Brünig M, Chyra O, Albrecht D, Driemeier L, Alves M (2008), A ductile damage criterion at various stress triaxialities, International journal of plasticity, 24: 1731-1755. https://doi.org/10.1016/j.ijplas.2007.12.001.

[24] Zadpoor A. A,Sinke J, Benedictus R (2009), Formability prediction of high strength aluminum sheets, International Journal of Plasticity, 25: 2269-2297. https://doi.org/10.1016/j.ijplas.2009.02.005.

[25] Gurson A. L (1977), Continuum theory of ductile rupture by void nucleation and growth: Part I-Yield criteria and flow rules for porous ductile media, 99(1): 2-15. https://doi.org/10.1115/1.3443401.

[26] Tvergaard V (1989), Material failure by void growth to coalescence, Advances in Applied Mechanics, 27: 83-151. https://doi.org/10.1016/S0065-2156(08)70195-9.

[27] Li H, Fu M, Lu J, Yang H (2011), Ductile fracture: Experiments and computations, International journal of plasticity, 27: 147-180. https://doi.org/10.1016/j.ijplas.2010.04.001.

[28] Lemaitre J (1985), A continuous damage mechanics model for ductile fracture, Journal of engineering materials and technology, 107: 83-89. https://doi.org/10.1115/1.3225775.

[29] Chaboche J. L (1981), Continuous damage mechanics-a tool to describe phenomena before crack initiation, Nuclear engineering and design, 64: 233-247. https://doi.org/10.1016/0029-5493(81)90007-8.

[30] Kachanov L (1958), Time of the Rupture Process under creep condition, Izvestia Akademii Nauk, SSSR, Technicheskikh Nauk, 8: 26-31. https://www.scirp.org/reference/referencespapers?referenceid=1910907.

[31] Gilioli A, Manes A, Giglio M, Wierzbicki T (2015), Predicting ballistic impact failure of aluminium 6061-T6 with the rate-independent Bao–Wierzbicki fracture model, International Journal of impact engineering, 76: 207-220. https://doi.org/10.1016/j.ijimpeng.2014.10.004.

[32] Kim J. H, Kim N. H, Kim Y. J, Hasegawa K, Miyazaki K (2013), Ductile fracture simulation of 304 stainless steel pipes with two circumferential surface cracks, Fatigue and Fracture of Engineering Materials and Structures, 36: 1067-1080. https://doi.org/10.1111/ffe.12072.

[33] Ruiz de Sotto M, Doquet V, Longère P, Papasidero J (2022), Anisotropic, rate-dependent ductile fracture of Ti-6Al-4V alloy, International Journal of Damage Mechanics, 31: 374-402.

https://doi.org/10.1177/10567895211036491.

[34] Miehe C, Teichtmeister S, Aldakheel F (2016), Phase-field modelling of ductile fracture: a variational gradient-extended plasticity-damage theory and its micromorphic regularization, Philos Trans A Math Phys Eng Sci, 374: 2066 . 10.1098/rsta.2015.0170.

[35] Mei J, Xing S, Vasu A, Chung J, Desai R, Dong P (2020), The fatigue limit prediction of notched components–A critical review and modified stress gradient based approach, International Journal of Fatigue, 135: 105531. https://doi.org/10.1016/j.ijfatigue.2020.105531

[36] Saji R. P, Pantidis P, Svolos L, Mobasher M. E (2025), Multi-stage calibration framework for continuum damage mechanics models, Engineering Fracture Mechanics, 326: 111341. https://doi.org/10.1016/j.engfracmech.2025.111341